Journal of Alloys and Compounds 1050 (2026) 185784

Contents lists available at ScienceDirect

Journal of Alloys and Compounds

journal homepage: www.elsevier.com/locate/jalcom

Structural, morphological, and functional characterization of $LaMnO_3$ nanoparticles synthesized via the reverse micelle method

Abdullah Hassan [a,b,*], Vanni Lughi [a]

[a] Department of Engineering and Architecture, University of Trieste, Trieste 34127, Italy
[b] Department of Physics, Faculty of Education, Albaydha University, Albaydha, Yemen

ARTICLE INFO

Keywords:
Reverse micelle synthesis
Perovskite oxides
Morphological analysis
Electrical conductivity
Small polaron hopping
Soft ferromagnetism

ABSTRACT

$LaMnO_3$ (LMO) nanoparticles were synthesized using the reverse micelle route and thoroughly characterized to determine their structural, morphological, optical, electrical, and magnetic properties. The single-phase formation of a cubic deformed perovskite structure with good crystallinity was confirmed by X-ray diffraction (XRD) and Rietveld refinement. Irregularly shaped nanoparticle agglomeration with a porous morphology was observed by scanning electron microscopy (SEM), and a homogeneous elemental distribution and phase purity were confirmed through energy-dispersive X-ray spectroscopy (EDS). Fourier-transform infrared (FTIR) spectroscopy complemented the characteristic Mn–O vibrational modes, allowing the stabilization of the well-defined MnO_6 octahedra. UV–visible spectroscopy indicated a direct optical bandgap of approximately 1.96 eV, suggesting its potential for use in visible-light-driven electronics. Electrical resistivity measurements exhibited thermally activated behavior with an activation energy of 0.21 eV, which is compatible with small polaron hopping in perovskite oxide semiconductors. Magnetic measurements at room temperature revealed that the size-induced surface effects and oxygen vacancies caused weak ferromagnetism.

1. Introduction

Perovskite-type oxides, which have the general formula ABO_3, are widely used in both research and industry because of their unique physical properties and flexibility. In these materials, the A-site is often filled by an alkali metal, alkaline earth metal, or a lanthanide element, whereas the B-site is mostly occupied by transition metal. For instance, Lanthanum Manganite (LMO) has a distorted perovskite structure with La^{3+} at the A-site, Mn^{3+} at the B-site, and O^{2-} ions grouped around the Mn in octahedral groups [1–6]. The diagram in Fig. 1 shows a structure with MnO_6 octahedra sharing corners, La atoms at the corners, Mn at the center, and oxygen at the edges. The perovskite structure is interesting because it can be chemically altered significantly, allowing us to fine-tune its electrical, magnetic, catalytic, and optical properties. Researchers are particularly interested in manganites, which are typically denoted as R1-xAxMnO3. In this formula, R represents a trivalent rare-earth ion, such as La, Pr, Y, or Nd, and A represents a divalent alkaline earth ion, such as Sr, Ca, or Ba [7–12]. We often replace some of the cations at either the A or B sites, which helps boost their effectiveness for different technological applications, such as solid oxide fuel cells, sensors, superconductors, and solar cells [13,14].

Perovskite oxides, especially those based on lanthanum, have gained significant attention owing to their diverse physical properties and potential applications in fields such as catalysis, sensors, fuel cells, and spintronic devices. Lanthanum manganite ($LaMnO_3$) is well-known for its unique magnetic and electrical properties, which vary depending on the structural shifts and fabrication. It has a slightly distorted perovskite structure, where the Mn^{3+} ions and oxygen octahedra affect the charges, spins, and orbitals of the material.

Compared to some perovskite materials with B atoms (such as manganese or titanium), which have more A-site defects, perovskite compounds contain fewer B-site cation faults and interstitial oxygen [15,16]. The main defects in these materials usually originate from issues with A-site cations and oxygen vacancies. We can store charges in perovskites using these oxygen vacancies, which are related to pseudo-capacitance [17].

Optimizing the synthesis method is critical for enhancing the morphology, phase purity, and functional properties of LMO. Reverse micelle method has a special advantage because it confines reactions to small areas, allowing for better control over particle size and uniformity. This technique is useful for fabricating nanostructured oxides with specific features.

* Corresponding author at: Department of Engineering and Architecture, University of Trieste, Trieste 34127, Italy.
E-mail address: ahassan@ictp.it (A. Hassan).

https://doi.org/10.1016/j.jallcom.2025.185784
Received 28 July 2025; Received in revised form 1 December 2025; Accepted 22 December 2025
Available online 23 December 2025

In this study, we investigated the use of the reverse micelle method for the production of LMO nanoparticles. We examined their structure using X-ray diffraction (XRD), shape and makeup using scanning electron microscopy (SEM) and energy-dispersive X-ray spectroscopy (EDS), and vibratory behavior using Fourier-transform infrared (FTIR) spectroscopy. We also investigated their optical properties using UV–vis spectroscopy and their electrical and magnetic properties using resistivity and magnetization testing. This study provides insights into the relationship between the LMO structure and its characteristics, demonstrating its potential for increased functionality in future studies.

Finally, we synthesized LMO nanoparticles using the reverse micelle method and analyzed their structural, morphological, and functional properties using various techniques. By changing the synthesis conditions and using advanced methods for analysis, we aim to identify clear links between the synthesis and performance of these materials. This is useful for designing LMO-based nanomaterials for specific applications.

2. Experimental

The synthesis of LMO compounds via the reverse micelle (RM) approach involves unconfined co-precipitation, followed by annealing to produce the desired perovskite phase [11,18,19]. Fig. 2 shows the process starting with the synthesis of two separate RM solutions in an iso-octane (nonpolar solvent), cetyltrimethylammonium bromide (CTAB, surfactant), n-butyl alcohol (co-surfactant), and water (polar phase) quaternary microemulsion system. The first microemulsion (RM1) contained a stoichiometric proportion of $La(NO_3)_3{\cdot}6H_2O$ and $Mn(NO_3)_2$ in water (0.1 M), and the second microemulsion (RM2) contained an equimolar aqueous solution of NaOH (0.1 M) under comparable conditions.

When RM1 and RM2 are mixed with constant stirring, intermicellar exchange and micellar fusion allow the metal and hydroxide ions to react with each other in the restricted aqueous cores, resulting in the regulated co-precipitation of mixed metal hydroxides. The processes are as follows:

$$La^{3+} + Mn^{2+} + OH^{-} \longrightarrow La(OH)_3.Mn(OH)_2\downarrow$$

The black suspension indicated the formation of a mixed hydroxide precursor. The slow addition of aqueous ammonia (NH_3) controls the pH to stabilize precipitation and prevent agglomeration. Ammonia is a secondary complexing agent that regulates ion release and homogeneity.

The precipitated product was isolated by microemulsion breaking via centrifugation and then thoroughly washed with ethanol and distilled water to remove the surfactants and excess residues. The powder was separated and dried at 80 °C for 6 h to evaporate water and volatile organics. After 5 h of calcination at 750 °C in air, the hydroxide precursor decomposed by solid-state diffusion to produce phase-pure LMO through the following overall transformation:

$$La(OH)_3 + Mn(OH)_2 \xrightarrow{750\ C^{\circ}} LaMnO_3 + 3H_2O\uparrow$$

This heat-accelerated reaction converts Mn^{2+} to Mn^{3+} /Mn^{4+} under atmospheric air, stabilizing the perovskite structure of the LMO Toolkit. The reverse micelle process creates a constrained reaction environment that favors homogeneous nucleation, restricts particle growth, and ensures the greatest morphological homogeneity of the final LMO powder [19,20].

3. Structure properties

We began by examining lanthanum manganese oxide (LMO) using X-ray powder diffraction. XRD patterns were obtained at room temperature, spanning a 2θ range of 20° to 80°. The diffraction patterns indicated the presence of crystals forming in a cubic single-phase structure. The peak shape was fitted using the pseudo-Voigt function, which combines Gaussian and Lorentzian functions. Fig. 3 displays the Rietveld plots developed using the FullProf software [21], and illustrates the sample's crystalline structure along with the Rietveld refinement pattern. The peaks are well-fitted, indicating that the sample is free from secondary impurity phases, as demonstrated in this figure [11,22]. It turns out that the sample is entirely pure perovskite, without any detectable impurities, which is quite impressive. The pattern shows a slightly distorted cubic lattice, leaning toward rhombohedral symmetry, which corresponds to the Pm-3m (No. 221) space group. These peak positions are consistent with the reference data from the COD (No. 961531527) [23], indicating that the desired LMO phase was obtained. We observed major reflections at angles corresponding to the (100, 110, 111, 200, 210, 211, 200, 300, and 310) planes. The sharpness and intensity of these peaks indicate high crystallinity and well-defined grains. The absence of any sign of a second phase adds to the evidence of superb chemical purity of the synthesized material. The tilting of the MnO_6 octahedra causes rhombohedral distortion, which is common in many perovskites with this structure [24,25].

These results show that we made a pure, well-ordered layer of manganese oxide (LMO), and we are now ready to conduct more detailed tests. To determine the size of the crystallites, we examined the widths of the peaks from (100, 110, 111, 200, 210, 211, 200, 300, and 310). Utilizing the Scherrer equation [26–29], we can determine the size through the following method:

$$D = \frac{0.9\lambda}{\beta\cos\theta} \quad (1)$$

where λ is the wavelength of the Cu-K radiation ($\lambda_{Cu} = 1.5406$ Å), β the

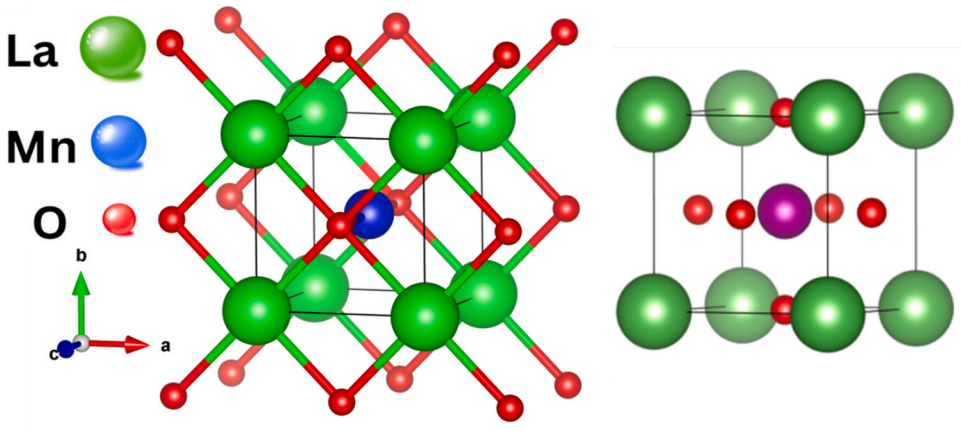

Fig. 1. Schematic of the crystal structure of $LaMnO_3$.

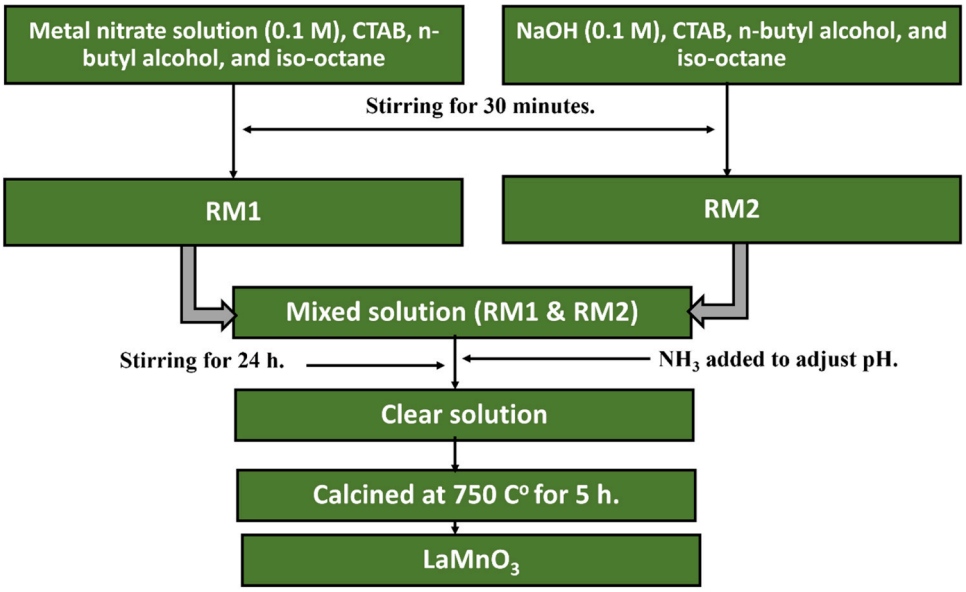

Fig. 2. A schematic representation of the synthesis route for $LaMnO_3$ nanoparticles via the RM method.

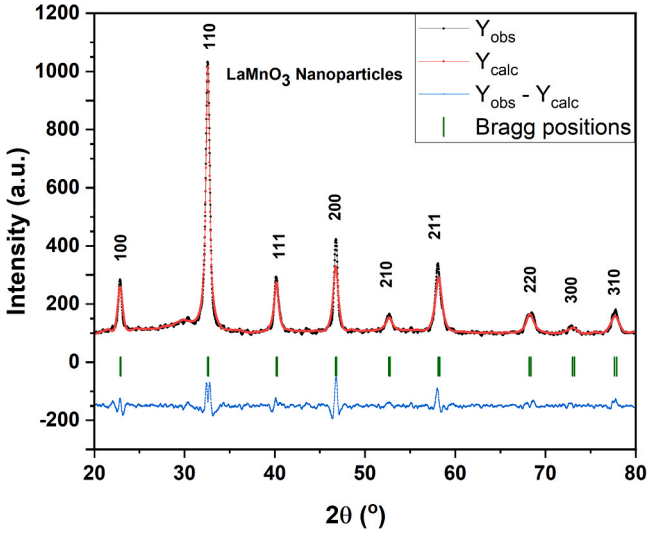

Fig. 3. XRD patterns of $LaMnO_3$ nanoparticles.

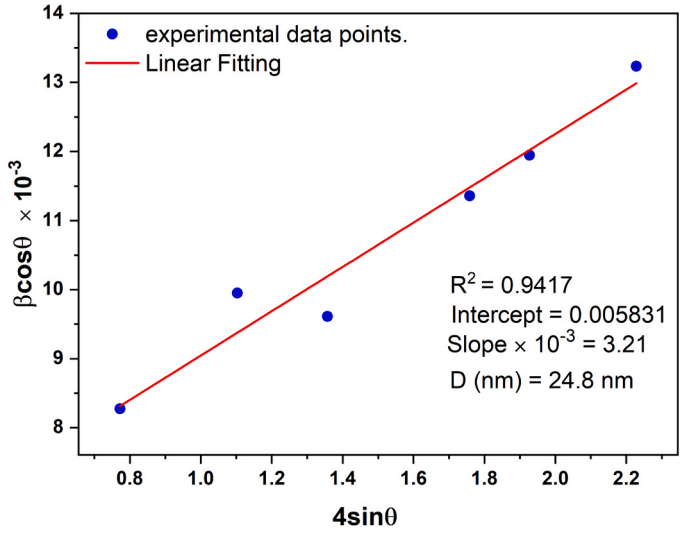

Fig. 4. W-H plot of the $LaMnO_3$ nanoparticles.

peak width, and θ the diffraction angle. This yielded lattice constants of a = b = c = 3.88 Å, a cell volume of V = 58.411 $Å^3$, and an average grain size of D = 14.9 nm.

The full width at half maximum (FWHM) was used to determine the peak broadening of nanoparticles caused by lattice strain and was expressed by the W–H (Williamson-Hall) relation, as shown below [26, 30–32]:

$$\beta\cos\theta = \frac{k\lambda}{D} + 4\varepsilon\sin\theta \quad (2)$$

In this case, β is the width of the strong XRD peak at half its height, θ is the diffraction angle, k is a shape factor constant, λ is the X-ray wavelength, D is the effective crystallite size, and ε is the lattice strain. To determine the micro-strain in the sample, the necessary calculations were conducted using the W–H plot. This involved utilizing the intercept and slope values from the linear fit between βcosθ and 4sinθ, as depicted in Fig. 4. From the straight-line nature of the Williamson-Hall plot, the intercept gives us D, while the slope shows ε. Linear fitting of our data yielded D = 24.9 nm and ε = 3.21, respectively. While the classic Scherrer equation yielded a smaller size of 14.9 nm, the W-H method yielded a larger size of 24.9 nm, which hints at some measurable microstrain that the Scherrer method overlooked.

3.1. Morphological and compositional analysis

We examined the shape and size of the LMO using a scanning electron microscope, and the results are shown in Fig. 5a. The particles were clumped together and had rough and irregular shapes. This is typical for this method because the growth space is compressed into tiny water pockets. The grains look like they are just loosely stacked and have this sponge-like skin, which should really help when it comes to doing surface chemistry or moving ions around. Most of the particles fall into the sub-micron size category, but when we zoom in more, we can see finer details at the nanoscale level. This suggests that although there was some randomness in the process, nucleation and growth were not random.

The crystallite size was approximately 19.2 nm, as measured from the micrograph using ImageJ software, and its size-dependent frequency

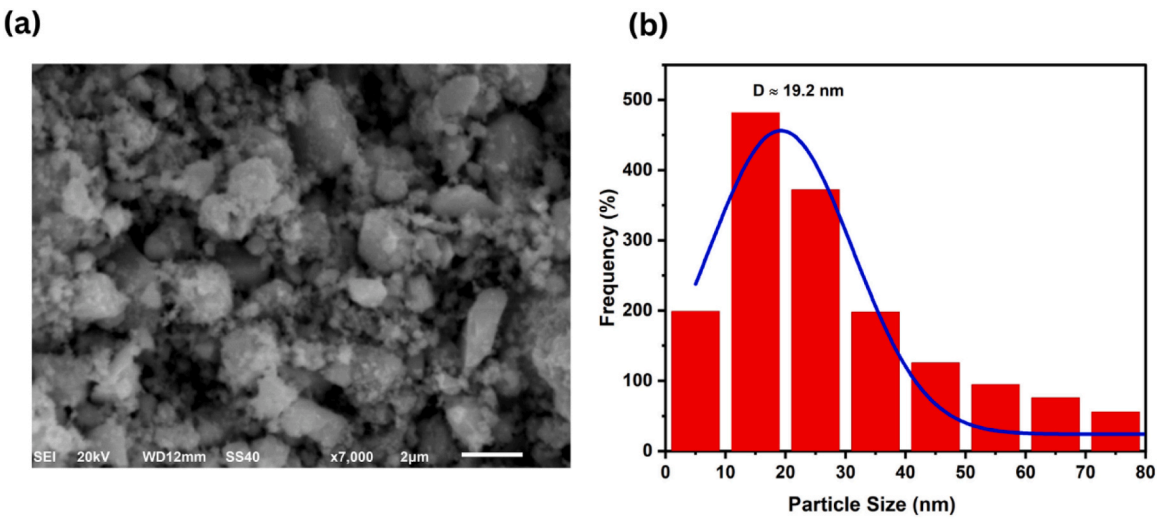

Fig. 5. a) SEM images of $LaMnO_3$ nanoparticles. b) Size distribution histograms of $LaMnO_3$ nanoparticles.

was illustrated using histograms [27]. The average sizes of crystallites were calculated by applying a Gaussian function to fit the size distribution histogram. [33]. The best-fitted histograms for the nanoparticles are shown in Fig. 5b and are consistent with those of the previous studies. [34,35]. It fits snugly between the two estimates obtained from XRD. Therefore, the grains observed in the SEM images are likely to be isolated single crystals or small groups composed of only a few grains. This supports the idea that the W-H- method provides a more complete picture of the crystallite size in strained nanostructures.

Fig. 6 shows the energy-dispersive X-ray spectroscopy results, which were used to determine the chemical compositions of the samples. The spectrum clearly shows La, Mn, and oxygen, with no signs of any unwanted elements. The elemental maps also show that La and Mn are evenly spread throughout the material, indicating that there was solid mixing down to the nanoscale. The amounts of these elements matched our expectations for LMO, indicating that it was a single-phase perovskite material. This is consistent with what we found in the X-ray diffraction patterns. Therefore, the SEM and EDS results provide a solid picture of well-formed LMO.

3.2. FTIR analysis

We performed Fourier-transform infrared spectroscopy in the wavelength range of 400–4000 cm^{-1} on the LMO perovskite sample produced by the reverse micelle method and heated it to 750 °C. The results are presented in Fig. 7. The spectrum shows the FTIR bands at 438, 615, 865, 1115, 1380, 1438, 1530, 1630, and 3436 cm^{-1}. Some clear absorption features appeared below 1000 cm^{-1}, which matched the metal-oxygen backbone, which is typical of many perovskite oxides [36,37]. The FTIR spectrum exhibits two main bands at approximately 438 and 615 cm^{-1} , which correspond to the characteristic vibrations of the MnO_6 octahedra. The band near 438 cm^{-1} arises from O-Mn-O bending [38], while the band around 615 cm^{-1} is attributed to Mn-O stretching [38], reflecting the Jahn-Teller distortion of Mn^{3+} [39,40]. The band at 1113 cm^{-1} was caused by the stretching vibrations of the C–O band of n-butanol $C_4H_{10}O$ [41]. These features confirm the formation of the perovskite LMO structure. In addition to the intrinsic lattice vibrations, minor absorption bands at 1382, 1440, and 1536 cm^{-1} are related to the stretching vibrations of residual nitrate

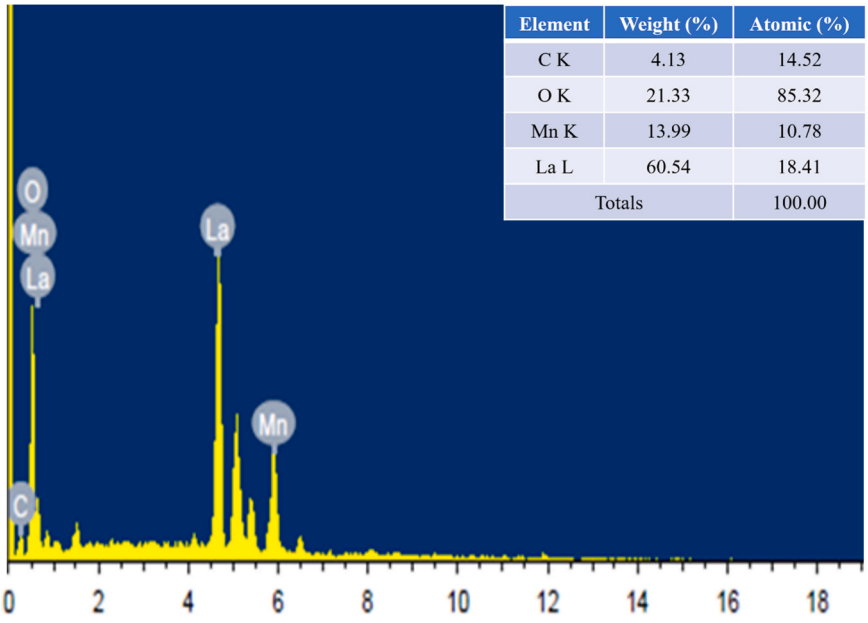

Element	Weight (%)	Atomic (%)
C K	4.13	14.52
O K	21.33	85.32
Mn K	13.99	10.78
La L	60.54	18.41
Totals		100.00

Fig. 6. EDS spectra of $LaMnO_3$ nanoparticles.

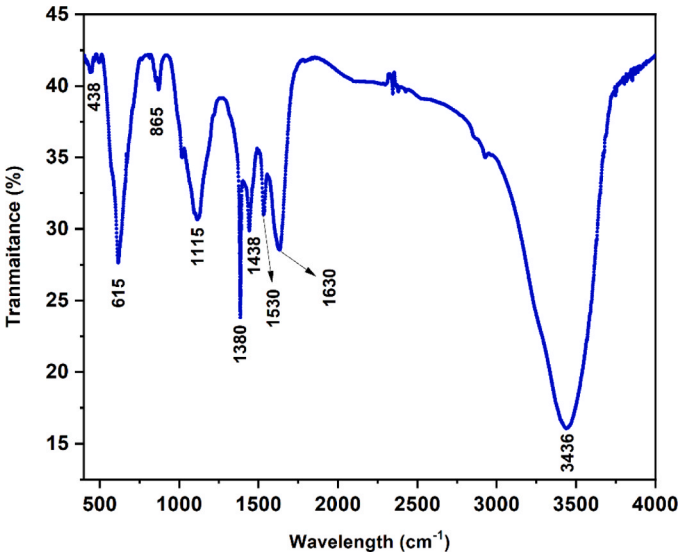

Fig. 7. FTIR spectra of $LaMnO_3$ nanoparticles.

(NO_3^-) or carbonate (CO_3^{2-}) groups due to the incomplete decomposition of metal nitrate precursors or CO_2 adsorption from ambient air on the surfaces of the nanoparticles [42,43].

The band at approximately 1627 cm^{-1} is attributed to the bending vibration of surface-adsorbed water [39]. We also observed a broad band around 3436 cm^{-1}, which can be easily linked to the O-H stretch and H-O-H bending modes [44]. The bands at approximately 1627 and 3436 cm^{-1} usually originate from water molecules or hydroxyls that are trapped on the powder surface after being exposed to air. The FTIR data confirmed that we produced a pure phase of LMO with a strong perovskite lattice, and organic impurities were almost nonexistent.

3.3. Optical properties

Much research on optical materials has focused on the interactions between electromagnetic waves, solids, and electric fields. Absorption spectroscopy is a common method for examining the optical properties of semiconductors. Several factors can affect the absorbance, such as the band gap, oxygen deficiency, surface roughness, and impurity centers.

We measured the UV–visible absorbance spectra of the LMO sample over wavelengths ranging from 200 to 800 nm, using distilled water as our reference. The results are shown in Fig. 8, which shows that the absorption spectrum has two distinct peaks. The first peak indicates that LMO nanoparticles may function well as photocatalytic materials, whereas the second peak is related to the reaction of LMO nanoparticles with visible light. To calculate the band gap of the sample, we used Tauc's relation [21] as follows:

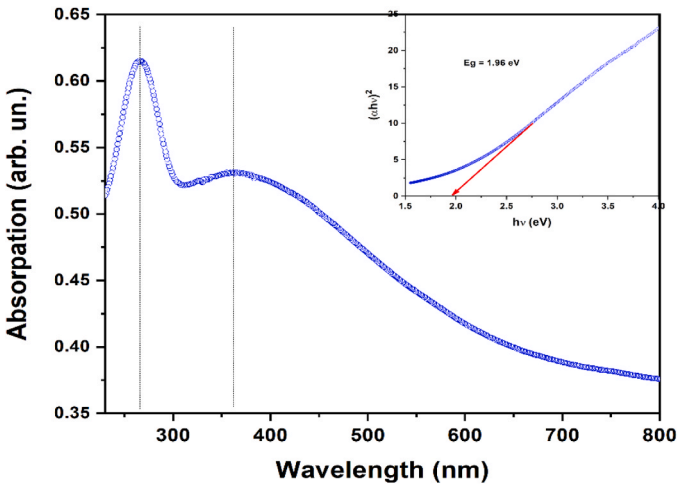

Fig. 8. UV–visible absorbance spectra of the $LaMnO_3$ nanoparticles. The inset shows the Tauc plots for the same.

$$(\alpha h\nu)^2 = C(h\nu - E_g) \tag{3}$$

Here, C is a constant, $h\nu$ is the photon energy, and n can take values of 1/2, 3/2, 2, and 3, depending on the electronic transition that causes the absorption. where α is the absorption coefficient, which is calculated as follows:

$$\alpha = 2.303\left(\frac{A}{d}\right) \tag{4}$$

where A is the absorbance, and d is the cuvette thickness. To determine the band gap of LMO, we plotted $(\alpha h\nu)^2$ against photon energy $(h\nu)$ for a direct transition, as shown in the inset of Fig. 8.

The optical bandgap of the LMO nanoparticles was determined to be 1.96 eV, which is marginally lower than the previously reported values [11,22,45]. This reduction in the bandgap is primarily attributed to oxygen vacancies [33], which introduce localized defect states within the forbidden energy gap, thereby facilitating electronic transitions at lower energy levels. The presence of mixed-valence Mn^{3+}/Mn^{4+} states, resulting from oxygen deficiency, modifies the Mn–O–Mn bond network and decreases the charge transfer energy between the O-2p and Mn-3d orbitals, thereby narrowing the bandgap [33,46]. Additionally, the nanoscale size of the particles leads to increased surface disorder and induces local lattice strain, which alters the MnO_6 octahedral distortion and consequently reduces the effective band gap.

The effective band gap (E*) for spherical particles is proportional to the average particle size R, and there is a formula for that too.

$$E^* = E_g^{bulk} = \frac{h^2\pi^2}{2eR^2}\left(\frac{1}{m_e m_o} + \frac{1}{m_h m_o}\right) - \frac{1.8e}{4\pi\varepsilon\varepsilon_o R} - \frac{0.124e^3}{\hbar^2(4\pi\varepsilon\varepsilon_o)^2}\left(\frac{1}{m_e m_o} + \frac{1}{m_h m_o}\right)^{-1} \tag{5}$$

Where E_g^{bulk} represents the bulk band gap, m_e is the electron effective mass, m_h is the hole effective mass, m_o is the free electron mass, ε is the relative permittivity and ε_o is the permittivity of free space.

3.4. Electrical properties

Fig. 9 shows the resistivity, ρ(T), of LMO changes between 280 and 580 K. The graphs show that LMO behaves as an insulator throughout the entire measured range. We can also see that at any given temperature, it behaves similarly to Lanthanum-based manganites, which we discussed in prior works [11]. However, there is a twist: LMO made using a different method exhibits more semiconductor-style behavior in terms of resistivity and temperature. As the temperature increases, the resistivity decreases, which is classic evidence of thermally activated conduction. What happens is that When the temperature increases, the electronic bandwidth expands, and the overlap between Mn_{3d} and O_{2p} increases. This indicates that electrons are more likely to jump from Mn^{3+} to Mn^{4+}, thereby increasing the conductivity of LMO, as shown in the inset of Fig. 9 [42]. The Arrhenius plot of ln(ρ) versus 1000/T yields a straight line, allowing us to calculate an activation energy (E_a) of approximately 0.21 eV. Furthermore, the values obtained from the temperature-dependent resistivity data correspond to those calculated using the Arrhenius equation:

$$\rho(T) = \rho_o \exp\left(\frac{E_a}{kT}\right) \tag{6}$$

Here, E_a represents the activation energy, ρ_o is a constant, k is

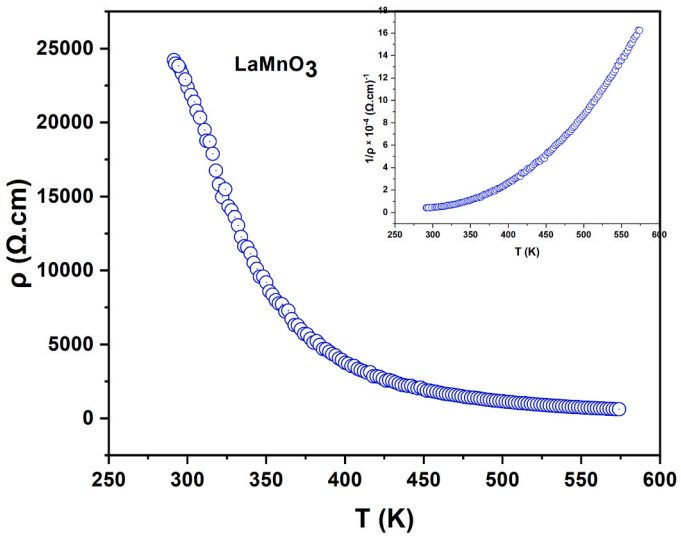

Fig. 9. Temperature-dependent resistivity variation of $LaMnO_3$ nanoparticles. The inset shows the temperature-dependent conductivity variation.

Boltzmann's constant, and T is the temperature in kelvins. We determined that the E_a from the slope of the Arrhenius plot in Fig. 10 indicates that E_a is approximately 0.21 eV. This is consistent with other studies on LMO, which typically have activation energies between 0.18–0.25 eV. [11,42,43]. This gives us more confidence in our findings, as it is consistent with previous studies, implying that small polaron hopping is the main mode of conductivity in our sample, as it is in LMO and other insulating perovskite manganites.

3.5. Magnetic properties

We investigated the magnetic characteristics of the synthesized LMO nanoparticles using a vibrating sample magnetometer (VSM) at room temperature (RT). The paramagnetic behavior of lanthanum manganite at room temperature can be attributed to several factors, such as a lack of oxygen, charge ordering, strong electron interactions, and its unique crystal structure [31]. The magnetic behavior of LMO is affected by the exchange interactions between Mn spins within the perovskite structure. In stoichiometric LMO, Mn^{3+} serves as a Jahn-Teller ion with a $t_{2g}^3 \quad e_g^1$ electron configuration, leading to a ground state with an A-type antiferromagnetic (AFM) arrangement. In this configuration, the interactions within the plane are ferromagnetic, whereas those between planes are antiferromagnetic [47,48].

As shown in Fig. 11, the M–H hysteresis loop exhibits a narrow S-shaped curve with very low remanence and coercivity, indicating weak ferromagnetic behavior against a predominantly antiferromagnetic background. Quantitatively, the nanoparticles exhibited a saturation magnetization of Ms = 0.76 emu·g^{-1} , remanent magnetization of Mr = 0.0012 emu·g^{-1} , and coercivity of Hc = 28.5 Oe. Conversely, Suresh et al. [31] detected room-temperature ferromagnetism in pure LMO nanoparticles, noting a significantly higher saturation magnetization (Ms) of approximately 4.22 emu·g^{-1} , a lower remanent magnetization (Mr) of approximately 0.000594 emu·g^{-1} , and a significantly reduced coercivity (Hc) of approximately 6.26 Oe in particles with an average size of approximately 30 nm.

Overall, the comparison indicated that the particle size plays a crucial role in determining the magnetic characteristics of LMO nanoparticles. Smaller LMO particles exhibited a lower saturation magnetization but enhanced coercivity, underscoring the typical interaction between surface disorder and intrinsic double-exchange ferromagnetism in nanoscale LMO systems [42]. These results further support the commonly observed size-dependent magnetic variations in rare-earth manganite nanoparticles.

This magnetic response differs significantly from the typical A-type antiferromagnetic ordering of bulk LMO, confirming that reducing the crystallite size to the nanoscale strongly modifies the magnetic ground state of the material significantly. The observed weak ferromagnetism was attributed to the coexistence of FM and AFM phases, which is a well-known phenomenon in nanosized Mn oxide systems. [49–52]. We interpret our results within a core–shell magnetic model, where the inner core retains the parent AFM order, while the outer shell, which is rich in structural distortions, defective oxygen sites, and broken exchange pathways, contains uncompensated and canted spins that collectively produce a soft ferromagnetic-like contribution to the magnetic moment of the system.

Spin canting is further enhanced by the Dzyaloshinskii–Moriya (DM) interaction [53], which becomes prominent owing to the distortion and tilting of MnO_6 the octahedra. Additionally, oxygen-vacancy-induced Mn^{3+}/Mn^{4+} mixed valence facilitates local double-exchange interactions, forming small ferromagnetic clusters embedded in the AFM matrix. These structural and electronic inhomogeneities create an FM shell coupled to an AFM core, explaining the small but finite Ms and very low Hc.

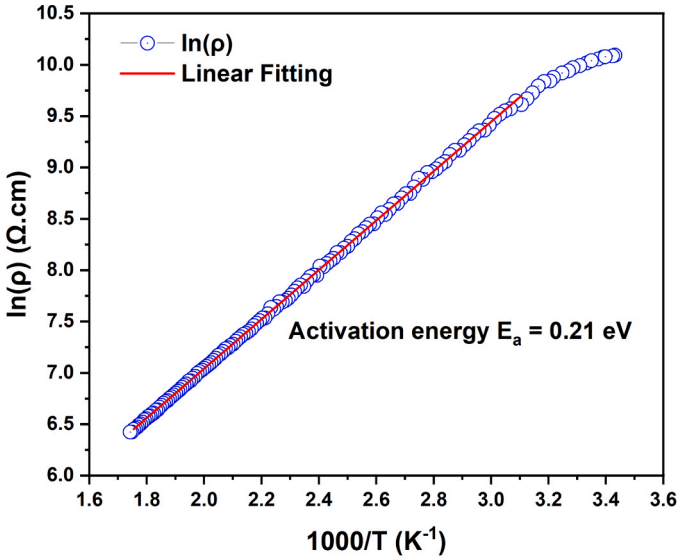

Fig. 10. Activation energy, Ea, of the $LaMnO_3$ nanoparticles.

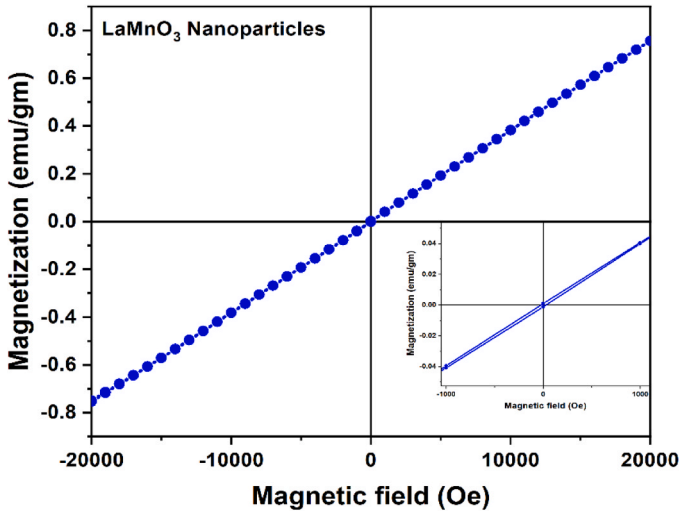

Fig. 11. M-H loops for $LaMnO_3$ nanoparticles. The inset shows a magnified view of the low-field region.

The hysteresis curve is also non-saturating, even at high fields, confirming the presence of AFM or paramagnetic components that remain unsaturated under an applied field. This linear high-field tail indicates that the total magnetization contains both a ferromagnetic component and an additional linear background; therefore, subtracting the linear term is required to accurately determine the intrinsic ferromagnetic saturation magnetization.

Overall, the magnetic behavior of these reverse-micelle-derived LMO nanoparticles arises from the interplay of finite-size effects, surface disorder, Mn^{3+}/Mn^{4+} mixed valence, and DM-induced canting, all of which contribute to the observed weak ferromagnetism of the nanoparticles. Based on the extracted Ms value, we estimated that the ferromagnetic volume fraction constituted only a few percent of the total magnetic content, which is consistent with the proposed core–shell magnetic-structure model.

4. Conclusions

$LaMnO_3$ (LMO) nanoparticles were successfully prepared by the reverse micelle route in the form of single-phase nanocrystalline perovskite structures with compositional uniformity and homogeneous morphology. The XRD pattern established a single-phase rhombohedral perovskite structure without secondary phases, whereas the SEM and EDS results showed porous, agglomerated nanoparticles with a homogeneous elemental distribution. FTIR spectra established the integrity of the MnO_6 octahedral network, whereas UV–vis spectroscopy established a direct optical band gap value of 1.96 eV, indicating visible-light applications.

Thermally activated hopping of small polarons was revealed by temperature-dependent resistivity measurements, with semiconducting behavior and an activation energy of 0.21 eV. Magnetic characterization revealed weak room-temperature ferromagnetism, which most probably resulted from surface spin disorder and size effects on the nanoscale.

Overall, the reverse micelle route was found to be effective for tuning the particle size, crystallinity, and functional properties of LMO nanoparticles. These findings make LMO a viable candidate for use in catalysis, optoelectronic devices, magnetic sensors, and spintronics.

CRediT authorship contribution statement

Abdullah Hassan: Writing – review & editing, Writing – original draft, Methodology, Investigation, Formal analysis, Data curation, Conceptualization. **Vanni Lughi:** Writing – review & editing, Supervision.

Declaration of Competing Interest

We wish to declare that there are no conflicts of interest associated with this article and we confirm that the manuscript is original and has not been previously published, is not currently submitted for review to any other journal and will not be submitted elsewhere before a decision is made by this journal.

Acknowledgments

The author, Abdullah Hassan, acknowledges the receipt of a fellowship from the ICTP TRIL SAR Programme for Training and Research in Italian Laboratories, Trieste, Italy, and the American Physical Society (APS), with additional support from Alfred P. Sloan Foundation. Special appreciation is extended to Ms. Leona Binz, my case manager at Scholars At Risk (SAR), and her colleagues for their unwavering support and assistance throughout the process.

References

[1] M. Humayun, Z. Li, M. Israr, A. Khan, W. Luo, C. Wang, Z. Shao, Perovskite type ABO_3 oxides in photocatalysis, electrocatalysis, and solid oxide fuel cells: state of the art and future prospects, Chem. Rev. 125 (2025) 3165–3241.
[2] C. Sun, J.A. Alonso, J. Bian, Recent advances in perovskite-type oxides for energy conversion and storage applications, Adv. Energy Mater. 11 (2021) 2000459.
[3] L. Lu, M. Sun, T. Wu, Q. Lu, B. Chen, C. Hei Chan, H. Ho Wong, Z. Li, B. Huang, Perovskite oxides for electrocatalytic hydrogen/oxygen evolution reaction, ChemElectroChem (2025) e202400648.
[4] C. Yang, Y. Tian, C. Yang, G. Kim, J. Pu, B. Chi, Recent progress and future prospects of anions O-site doped perovskite oxides in electrocatalysis for various electrochemical systems, Adv. Sci. 10 (2023) 2304224.
[5] J.M. Gallmetzer, F.R.S. Purtscher, J. Gamper, A. Mohammadi, R. Feyerherm, W. Riedel, S. Penner, T.S. Hofer, Combined experimental and theoretical approach to the electronic and magnetic properties of Cu-doped LaMnO3 perovskites, J. Phys. Chem. C 129 (2024) 677–688.
[6] C.J. Fu, Q. Ma, L. Gao, S. Li, Recent advances in perovskite oxides electrocatalysts: ordered perovskites, cations segregation and exsolution, ChemCatChem 15 (2023) e202300389.
[7] B. Munisha, L. Patra, J. Nanda, S. Mondal, Insights into the electronic, magnetic structure, and photocatalytic activity of Y_2CuMnO_6 double perovskite, RSC Adv. 15 (2025) 3110–3121, https://doi.org/10.1039/d4ra06357k.
[8] P.R. Nadig, O. Toulemonde, P. Alagarsamy, M.S. Murari, M.D. Daivajna, Multifaceted roles of Ag+ ions within and outside La–Ca–MnO_3 perovskite manganites: unveiling the room temperature magnetocaloric effect, J. Phys. Chem. C 128 (2024) 12686–12703.
[9] I.B. Sever, A.O. Ayaş, A. Kandemir, A. Ekicibil, Unveiling A-site substituent's influence on magnetocaloric response in $La_{2-x}Na_xNiMnO_6$ ($0.0 \leq x \leq 1.0$) double perovskite manganite materials, J. Sol. Gel Sci. Technol. (2025) 1–15.
[10] P. Chettri, B. Kunwar, G. Bhatt, S. Mangavati, A.K. Sarma, G.S. Okram, D. Chinnapareddy, A. Rao, U. Deka, Oxygen plasma-induced modification of structural and electrical properties of $Pr_{0.5}Sr_{0.5}MnO_3$ manganites, Phys. Status Solidi 221 (2024) 2400436.
[11] A.A.S. Hassan, W. Khan, S. Husain, P. Dhiman, M. Singh, Investigation of structural, optical, electrical, and magnetic properties of Fe-doped $La_{0.7}Sr_{0.3}MnO_3$ manganites, Int. J. Appl. Ceram. Technol. 17 (2020) 2430–2438.
[12] Z. Xie, C. Xu, X. Jiang, W. Zhang, M. Feng, S. Zhong, Z. Zou, Changes in $La_{0.8}Sr_{0.2}MnO_3$ manganites structure, magnetic and magnetocaloric properties by Pr^{3+} doping, Appl. Phys. A 130 (2024) 572.
[13] I.S. Steinberg, V.V. Atuchin, Two-photon holographic recording in $LiTaO_3$:Fe crystals with high intensity nanosecond pulses at 532 nm, Mater. Chem. Phys. (2020), https://doi.org/10.1016/j.matchemphys.2020.122956.
[14] I. Calisir, D.A. Hall, Chemical heterogeneity and approaches to its control in $BiFeO_3$–$BaTiO_3$ lead-free ferroelectrics, J. Mater. Chem. C 6 (2018) 134–146.
[15] H. Nan, X. Hu, H. Tian, Recent advances in perovskite oxides for anion-intercalation supercapacitor: a review, Mater. Sci. Semicond. Process 94 (2019) 35–50.
[16] Z. Xu, Y. Liu, W. Zhou, M.O. Tade, Z. Shao, B-site cation-ordered double-perovskite oxide as an outstanding electrode material for supercapacitive energy storage based on the anion intercalation mechanism, ACS Appl. Mater. Interfaces 10 (2018) 9415–9423.
[17] F. Hadji, M. Omari, M. Mebarki, N. Gabouze, A. Layadi, Zinc doping effect on the structural and electrochemical properties of $LaCoO_3$ perovskite as a material for hybrid supercapacitor electrodes, J. Alloy. Compd. 942 (2023) 169047.
[18] A.A.S. Hassan, W. Khan, S. Husain, P. Dhiman, M. Singh, M.M. Alanazi, Influence of Ni doping on physical properties of $La_{0.7}Sr_{0.3}FeO_3$ synthesized by reverse micelle technique, J. Mater. Sci. Mater. Electron 32 (2021) 3753–3765, https://doi.org/10.1007/s10854-020-05120-w.
[19] J. Eastoe, M.J. Hollamby, L. Hudson, Recent advances in nanoparticle synthesis with reversed micelles, Adv. Colloid Interface Sci. 128 (2006) 5–15.
[20] M.-P. Pileni, Recent advances in nanoparticle synthesis with reversed micelles, J. Phys. Chem. B 105 (2001) 3358–3371.
[21] J. Rodríguez-Carvajal, Recent advances in magnetic structure determination by neutron powder diffraction, Phys. B Condens. Matter 192 (1993) 55–69.
[22] A.A. Saad, W. Khan, P. Dhiman, A.H. Naqvi, M. Singh, Structural, optical and magnetic properties of perovskite $(La_{1-x}Sr_x)(Fe_{1-x}Ni_x)O_3$, (x = 0.0, 0.1 & 0. 2) nanoparticles, Electron. Mater. Lett. (2013), https://doi.org/10.1007/s13391-012-2103-1.
[23] S. Naray-Szabo, Die Strukturen von Verbindungen ABO_3,,Schwesterstrukturen, Naturwissenschaften 31 (1943) 466.
[24] J.A. Alonso, M.J. Martinez-Lope, M.T. Casais, M.T. Fernández-Díaz, Evolution of the Jahn− Teller distortion of MnO_6 octahedra in $RMnO_3$ perovskites (R= Pr, Nd, Dy, Tb, Ho, Er, Y): a neutron diffraction study, Inorg. Chem. 39 (2000) 917–923.
[25] M.A. Islam, J.M. Rondinelli, J.E. Spanier, Normal mode determination of perovskite crystal structures with octahedral rotations: theory and applications, J. Phys. Condens. Matter 25 (2013), https://doi.org/10.1088/0953-8984/25/17/175902.
[26] Anchal Sarita, Priya, S.R. Choudhary, M.S. Rulaniya, A. Kumar, S.N. Dolia, P. A. Alvi, B.L. Choudhary, Studies of structural, optical, and Raman analysis of Ni-substituted $CoFe_2O_4$, Phys. Status Solidi Appl. Mater. Sci. 221 (2024) 1–11, https://doi.org/10.1002/pssa.202400083.
[27] P. Scherrer, Bestimmung der Grosse und inneren Struktur von Kolloidteilchen mittels Rontgenstrahlen, Nach Ges. Wiss. Gottingen 2 (1918) 8–100.
[28] G.Lal, K. Punia, S.N. Dolia, P.A. Alvi, B.L. Choudhary, S. Kumar, Structural, Cation Distribution, Optical and Magnetic Properties of quaternary $Co_{0.4+x}Zn_{0.6-x}Fe_2O_4$

(x= 0.0, 0.1 and 0.2) and Li doped quinary $Co_{0.4+x}Zn_{0.5-x}Li_{0.1}Fe_2O_4$ (x= 0.0, 0.05 and 0.1) nanoferrites., Journal of Alloys and Compounds 828 (2020): 154388. https://doi.org/10.1016/j.jallcom.2020.154388.
[29] N. Dolia, P.A. Alvi, Low temperature field dependent magnetic study of the $Zn_{0.5}Co_{0.5}Fe_2O_4$ nanoparticles, J. Magn. Magn. Mater. 536 (2021) 168102, https://doi.org/10.1016/j.jmmm.2021.168102.
[30] K.K. Palsaniya, N. Kumari, S.N. Dolia, P.A. Alvi, B.L. Choudhary, Tailoring quantum dots through citric acid modulation of $CoFe_2O_4$ ferrite, Mater. Chem. Phys. 313 (2024) 128820, https://doi.org/10.1016/j.matchemphys.2023.128820.
[31] S. Suresh, P.S. Vindhya, V.T. Kavitha, A comprehensive study of dielectric, magnetic and anticancerous properties of lanthanum manganite perovskite nanoparticles, J. Alloy. Compd. 976 (2024) 173222, https://doi.org/10.1016/j.jallcom.2023.173222.
[32] G.K. Williamson, W.H. Hall, X-ray line broadening from filed aluminium and wolfram, Acta Met. 1 (1953) 22–31.
[33] A. Almohammedi, E.K. Abdel-Khalek, Y.A.M. Ismail, Investigation of structural, optical, magnetic, and electrochemical properties of $La_{1-x}Ag_xFe_{0.5}Mn_{0.5}O_{3-\delta}$ perovskites, Scientific Reports 15 1 (2025) 24463.
[34] V. Celorrio, L. Calvillo, C.A.M. van den Bosch, G. Granozzi, A. Aguadero, A. E. Russell, D.J. Fermín, Mean intrinsic activity of single Mn sites at $LaMnO_3$ nanoparticles towards the oxygen reduction reaction, ChemElectroChem 5 (2018) 3044–3051.
[35] A. Dutta, N. Gayathri, R. Ranganathan, Effect of particle size on the magnetic and transport properties of $La_{0.875}$ $Sr_{0.125}$ MnO_3, Phys. Rev. B 68 (2003) 54432.
[36] D. Kim, S. Townsley, V.H. Grassian, Vibrational spectroscopy as a probe of heterogeneities within geochemical thin films on macro, micro, and nanoscales, RSC Adv. 13 (2023) 28873–28884.
[37] S. Pasieczna-Patkowska, M. Cichy, J. Flieger, Application of Fourier transform infrared (FTIR) spectroscopy in characterization of green synthesized nanoparticles, Molecules 30 (2025) 684.
[38] M.S. Afify, M.M. El Faham, U. Eldemerdash, W.M.A. El Rouby, Room temperature ferromagnetism in Ag doped $LaMnO_3$ nanoparticles, J. Alloy. Compd. 861 (2021) 158570, https://doi.org/10.1016/j.jallcom.2020.158570.
[39] K.L. Damena, Investigation of Thermal, Structural and Electrical Properties of $LaMnO_{3\ -Sigma}$, 5 (2019) 48–55. https://doi.org/10.11648/j.ajn.20190504.14.
[40] N. Arjun, G. Pan, T.C.K. Yang, The exploration of Lanthanum based perovskites and their complementary electrolytes for the supercapacitor applications, Results Phys. 7 (2017) 920–926, https://doi.org/10.1016/j.rinp.2017.02.013.
[41] V. Brusko, A. Khannanov, A. Rakhmatullin, A.M. Dimiev, Unraveling the infrared spectrum of graphene oxide, Carbon N. Y. 229 (2024) 119507, https://doi.org/10.1016/j.carbon.2024.119507.
[42] A. Hernando, M.L. Ruiz-González, O. Diaz, J.M. Alonso, J.L. Martínez, A. Ayuela, J. M. González-Calbet, R. Cortés-Gil, Tuning magnetoconductivity in $LaMnO_3$ NPs through cationic vacancy control, Nanomaterials 13 (2023) 1601.
[43] A. Maignan, C. Martin, F. Damay, B. Raveau, J. Hejtmanek, Transition from a paramagnetic metallic to a cluster glass metallic state in electron-doped perovskite manganites, Phys. Rev. B 58 (1998) 2758.
[44] L.N. Moghadam, Z.R. Ranjbar, Cost-ef fi cient solar cells using nanocrystalline perovskite La (Fe and Mn)O_3 and candle soot: theory and experiment, J. Alloy. Compd. 785 (2019) 117–124, https://doi.org/10.1016/j.jallcom.2019.01.068.
[45] S. Gong, B. Liu, Electronic energy gaps and optical properties of $LaMnO_3$, Phys. Lett. A 375 (2011) 1477–1480, https://doi.org/10.1016/j.physleta.2011.02.027.
[46] M. Shaterian, M. Enhessari, D. Rabbani, M. Asghari, M. Salavati-Niasari, Synthesis, characterization and photocatalytic activity of $LaMnO_3$ nanoparticles, Appl. Surf. Sci. 318 (2014) 213–217, https://doi.org/10.1016/j.apsusc.2014.03.087.
[47] T.K. Bhowmik, S. Halder, T.P. Sinha, Tailoring the magnetic landscape in Al-doped $LaMnO_3$: an experimental and computational perspective, Phys. Scr. 98 (2023), https://doi.org/10.1088/1402-4896/acae41.
[48] M. Li, C. Tang, T.R. Paudel, D. Song, L. Weiming, K. Han, Z. Huang, S. Zeng, X. Renshaw Wang, P. Yang, Ariando, J. Chen, T. Venkatesan, E.Y. Tsymbal, C. Li, S.J, Pennycook, controlling the magnetic properties of $LaMnO_3/SrTiO_3$ heterostructures by stoichiometry and electronic reconstruction: atomic-scale evidence, Adv. Mater. 31 (2019) 1–8, https://doi.org/10.1002/adma.201901386.
[49] Y. Anahory, L. Embon, C.J. Li, S. Banerjee, A. Meltzer, H.R. Naren, A. Yakovenko, J. Cuppens, Y. Myasoedov, M.L. Rappaport, Emergent nanoscale superparamagnetism at oxide interfaces, Nat. Commun. 7 (2016) 12566.
[50] O. Gomonay, S. Kondovych, V. Loktev, Shape-induced anisotropy in antiferromagnetic nanoparticles, J. Magn. Magn. Mater. 354 (2014) 125–135.
[51] E. Hernández, V. Sagredo, G.E. Delgado, Synthesis and magnetic characterization of $LaMnO_3$ nanoparticles, Rev. Mex. F. íSci. 61 (2015) 166–169.
[52] V. Markovich, G. Jung, I. Fita, D. Mogilyansky, X. Wu, A. Wisniewski, R. Puzniak, L. Titelman, L. Vradman, M. Herskowitz, Magnetotransport properties of ferromagnetic $LaMnO_{3+\delta}$ nano-sized crystals, J. Magn. Magn. Mater. 322 (2010) 1311–1314.
[53] I. Dzyaloshinsky, A thermodynamic theory of "weak" ferromagnetism of antiferromagnetics, J. Phys. Chem. Solids 4 (1958) 241–255.